Materials Advances

ROYAL SOCIETY OF CHEMISTRY

PAPER

View Article Online
View Journal | View Issue

Cite this: *Mater. Adv.*, 2022, 3, 8579

Ultrathin CdS@BDC nanosheets derived from 2D metal–organic frameworks for enhanced photoinduced-stability and photocatalytic hydrogen production†

Jian Li,‡[ab] Huaqiang Wang,‡[b] Yihong Gao,[b] Hao Fang,[b] Peiyu Chen[b] and Fangzhi Huang *[b]

Two-dimensional metal–organic framework materials have attracted much attention due to their large surface area, porous structure and high carrier separation efficiency. Herein, we innovatively proposed a facile *in situ* vulcanization method, in which 2D Cd-MOF was used as the precursor and template to prepare a novel ultrathin CdS@1,4-benzenedicarboxylic (CdS@BDC) nanosheet in Na_2S/Na_2SO_3 solution. The obtained CdS@BDC nanosheet has the overall morphology of a 1.46 nm average thickness nanosheet skeleton, and is uniformly *in situ* embedded with CdS nanoparticles with an average size of 6 nm. Due to the two-dimensional skeleton structure, the efficiency of capture, separation and migration of photogenerated carriers was significantly improved. The hydrogen evolution rate (HER) of ultrathin CdS@BDC nanosheet photocatalysts is up to 13 081 μmol h^{-1} g^{-1}, which is 65 times higher than that of traditional CdS nanoparticles (199 μmol h^{-1} g^{-1}). The excellent photocatalytic performance of CdS@BDC nanosheets can be attributed to the inherited structural and functional advantages of 2D Cd-MOF. For example, the efficiency of photo-generated carrier capture, separation and migration is significantly improved. For another example, the surface of the photocatalyst can adsorb a large amount of S^{2-} ions, which not only consumes photogenerated holes as effective hole scavengers, but also accelerates the interfacial H_2-production reaction due to the effective H^+-capturing active sites. Thus, a tentative S^{2-}-mediated mechanism for the enhanced photoinduced-stability of CdS@BDC nanosheets was also proposed. The present work provides a facile and fascinating strategy for the synthesis of highly efficient photocatalysts.

Received 15th August 2022,
Accepted 24th September 2022

DOI: 10.1039/d2ma00866a

rsc.li/materials-advances

1. Introduction

With the excessive consumption of fossil fuels and the increasingly serious environmental pollution problem in the world, it is an important research topic to convert the inexhaustible solar energy into green chemical energy for the development of alternative energy.[1–6] Since Honda and Fujishima pioneered photocatalytic water splitting on TiO_2 electrodes in 1972,[7] solar-driven splitting of water for hydrogen production has gradually become a promising environmental route to achieve renewable and clean hydrogen energy. To date, extensive efforts have been focused on semiconductor materials such as g-C_3N_4,[8,9] $BiVO_4$,[10,11] Ta_3N_5,[12,13] CNPs@PEI-Co,[14] and CdS,[15–18] which have been widely used to develop photocatalysts for hydrogen evolution. CdS has been recognized as one of the most attractive photocatalytic materials for hydrogen evolution among the various photocatalysts owing to its superior optical properties (E_g = 2.4 eV) for efficiently absorbing visible-light, and appropriate conduction band level for the proton reduction reaction.[19,20] However, pure CdS still can't show gratifying photocatalytic activity due to its rapid photogenerated charge recombination and serious photocorrosion during the light irradiation reaction.[21–23] In addition, the limited active sites on the surface of unmodified CdS also restrict its catalytic activity.[24] To address the above shortcomings, the emergence of 2D nanostructures may be an effective way to inhibit the recombination of electron–hole pairs and provide more reactive sites.[25,26] More importantly, photogenerated electrons and

[a] *Department of Chemical and Chemical Engineering, Hefei Normal University, Hefei, 230601, P. R. China*
[b] *Lab of Clean Energy & Environmental Catalysis, Anhui Province Key Laboratory of Chemistry for Inorganic/Organic Hybrid Functionalized Materials, Institute of Physical Science and Information Technology, School of Chemistry and Chemical Engineering, Anhui University, Hefei 230601, P. R. China.*
E-mail: huangfangzhi@163.com; Tel: +86-551-63861328

† Electronic supplementary information (ESI) available. See DOI: https://doi.org/10.1039/d2ma00866a

‡ These authors contribute equally to this paper.

holes only need to overcome a short transmission distance to the surface of catalyst, and the separation efficiency can be greatly accelerated in 2D nanomaterials.

Recently, two-dimensional (2D) metal–organic frameworks (MOFs), a new class of organic–inorganic hybrid materials constructed by metal ions/clusters and organic ligands have been vastly investigated in catalysis fields.[27,28] Compared with other 2D nanomaterials such as graphene,[29] transition metal dichalcogenides (TMDs),[30] layered hydroxide[31] and black phosphorus,[32] the unique structural and compositional features of 2D MOFs, such as large surface area, abundant active sites, highly ordered porous structure and controllable composition, render them a promising template for creating 2D MOF-derived composite nanosheets.[33–35] For example, Qiao *et al.*[36] loaded CdS nanoparticles onto 2D Ni-based MOFs, which tremendously reduced the photocorrosion of CdS and the recombination of electrons and holes *via* electron transport from CdS to 2D Ni-based MOFs. Zhang *et al.*[37] reported a facile approach for the synthesis of CuS/Cu-TCPP composite nanosheets, exhibiting a remarkably increased photocurrent compared to the pure Cu-TCPP nanosheets. Liu *et al.*[38] synthesized 2D free-standing N-doped Ni-Ni_3S_2@carbon nanoplates by pyrolysis treatment from a precursor of Ni-based MOF nanoplates, which displayed a low overpotential of 284.7 mV at a current density of 10 mA cm^{-2} in alkaline solution. That is to say, metal sulfide associated with 2D MOF is a prospective strategy because of the following advantages: (i) the high surface area is capable of stabilizing the size and hindering the aggregation of nanoparticles; (ii) the ultrathin thickness results in a shorter transmission distance for photogenerated electrons reaching the surface of the catalyst, as well as reducing the recombination of electron–hole pairs; (iii) the large exposure of active sites is favorable for promoting the surface reduction of catalysts. However, to our knowledge, research on 2D MOFs in photocatalysis is still in its infancy. Based on various 2D MOFs, it remains a meaningful challenge to design and produce a more efficient system to enhance the photocatalytic performance by reducing the photocorrosion or producing more active sites of cadmium sulfide, *etc.*

Hence, we use 2D Cd-MOF nanosheets (NSs) as the precursor and template, and report a method of the *in situ* synthesis of CdS@1,4-benzenedicarboxylic (CdS@BDC) nanosheet (NS) photocatalysts based on the reaction of cadmium ions in the Cd-MOF skeleton and sulfur ions in Na_2S/Na_2SO_3 solution. In this study, the Na_2S/Na_2SO_3 system can not only be used as a precursor of sulfur ions for the rapid synthesis of CdS, but also can act as a hole sacrificial agent to prevent the photocorrosion of CdS in the process of the photocatalytic reaction. More importantly, the ultrathin skeleton of CdS@BDC NSs not only successfully regulated the distribution and size of CdS nanoparticles, but also continued the advantage of 2D to promote its catalytic performance. Due to the porous structure and large surface area of the synthesized CdS@BDC NSs derived from the 2D Cd-MOF, a large number of S^{2-} ions can be rapidly enriched to its surface, forming a S^{2-}-mediated layer to prevent the photocorrosion. As expected, the synthesized CdS@BDC NSs system has excellent stability and reusability, and its photocatalytic activity is 65 times higher than that of traditional CdS nanoparticles. It not only provides a facile and fascinating strategy for the synthesis of highly efficient photocatalysts, but also opens up a new insight for the application of 2D MOF-based nanomaterials in photocatalysis.

2. Experimental sections

2.1 Chemicals and materials

Cadmium acetate dehydrate ($Cd(CH_3COO)_2{\cdot}2H_2O$), *N*,*N*-dimethylformamide (DMF) and 1,4-benzenedicarboxylic acid (H_2BDC) were purchased from Shanghai Aladdin Biochemical Technology Co. Ltd. Sodium sulfide nonahydrate ($Na_2S{\cdot}9H_2O$), sodium sulfite (Na_2SO_3), cadmium chloride ($CdCl_2{\cdot}2.5H_2O$) and trisodium phosphate ($Na_3PO_4{\cdot}12H_2O$) were purchased from Shanghai Chemical Reagent Co. Ltd. All the reagents were of analytical grade and used without further purification. Ultrapure water with a resistivity of 18.2 MΩ cm was used throughout all the experiments.

2.2 Catalyst preparation

2.2.1 Synthesis of Cd-MOF nanosheets (NSs). Cd-MOF NSs were prepared *via* a solvothermal approach. Firstly, $Cd(CH_3COO)_2{\cdot}2H_2O$ (0.3731 g, 1.4 mmol) was dissolved in 30.0 mL of DMF to form a solution, which was subsequently added to 33.0 mL of DMF solution including H_2BDC (0.1163 g, 0.7 mmol). After strongly stirring at room temperature for 1 h, the mixed solution was poured into a 100 mL Teflon-lined autoclave. Then the autoclave was heated at 120 °C for 48 h, followed by cooling down to room temperature naturally. Finally, the resulting white precipitates were obtained after being filtered and washed with deionized water at least three times and dried under vacuum at 70 °C overnight.

2.2.2 Synthesis of CdS@BDC nanosheets (NSs). CdS@BDC NSs were prepared by an *in situ* synthesis method utilizing Cd-MOF nanosheets as the precursor and template. In detail, the as-prepared Cd-MOF NSs (5 mg) were rapidly added into 20.0 mL of mixing solution with 0.1 M Na_2S/Na_2SO_3, and then strongly stirred for 30 min. In this case, the amount of sulfur is far more than the amount of cadmium from Cd-MOF NSs. Therefore, after the complete consumption of cadmium for forming CdS@BDC NSs, there was still a rich Na_2S/Na_2SO_3 in the reaction system, which was directly utilized for the following photocatalytic H_2 production test. In order to describe the morphology and microstructures of the CdS@BDC NSs, the above mixed solution was filtered and washed with deionized water several times and then dried under vacuum at 50 °C overnight.

For comparison, CdS nanoparticles (NPs) were synthesized using a modified method.[39] Briefly, 30.0 mL of 0.1 M Na_2S solution was added into 30.0 mL of 0.1 M $CdCl_2{\cdot}2.5H_2O$ solution under stirring conditions. After vigorously stirring for 10 min, the achieved suspension was added dropwise into 2.0 mL of 0.05 M $Na_3PO_4{\cdot}12H_2O$ with stirring for 20 min. And then, the mixed solution was transferred into a 100 mL

Teflon-lined autoclave and kept at 180 °C for 12 h. The product was collected by filtration, washed with absolute ethanol and deionized water separately, and finally dried under vacuum at 60 °C overnight.

2.3 Characterization

Scanning electron microscopy (SEM) images were acquired using a Zeiss Supra 40 scanning electron microscope with an acceleration voltage of 5 kV, combined with energy dispersive X-ray (EDX) spectroscopy. A JEM-2010-TEM electron microscope (JEOL, Japan) was used to obtain the elemental mapping, TEM and HRTEM images. Atomic force microscopy (AFM) images were recorded using a Dimension Edge instrument. Powder X-ray diffraction (PXRD) patterns were analyzed on a Philips X'Pert PRO SUPER X-ray diffractometer equipped with graphite-monochromated Cu Kα radiation (λ = 1.54056 Å). An ESCALab MKII XPS spectrometer system with Al Ka (1486.6 eV) as the X-ray source was used to carry out the XPS measurements. UV-vis spectra were measured using a spectrophotometer (Hitachi U-4100). The steady-state photoluminescence (PL) spectra for liquid samples were conducted through HitachF-4500 under an excitation wavelength of 425 nm. A FS5 fluorescence lifetime spectrometer (Edinburgh Instruments, UK) was used to obtain the time-resolved PL decay curves under the excitation of 425 nm and probed at 475 nm.

2.4 Hydrogen evolution measurements

The photocatalytic H_2 production experiments were performed in a 100 mL Pyrex flask connected to a closed gas circulation and evacuation system under a 300 W Xe lamp (CEL-HFX300, Beijing China Education Au-light Co., Ltd) equipped with an optical cut-off filter ($\lambda > 380$ nm). In a typical experiment (apart from CdS@BDC NSs sample), 5 mg of the photocatalyst was dispersed in 20.0 mL of an aqueous solution including Na_2S (0.1 M) and Na_2SO_3 (0.1 M) as the sacrificial electron donors. Prior to irradiation, the suspension was stirred for 10 min and then bubbled with N_2 for 30 min to completely remove the dissolved air. Subsequently, the photocatalytic reactor was irradiated by a Xe lamp with a UV cut off filter (>380 nm) at a fixed distance (10 cm). Throughout the irradiation process, the above suspension was continuously stirred and kept at 6 °C through a flow of cooling water. The evolved H_2 was measured *via* gas chromatography (Shimadzu GC-2014C, N_2 as a carrier gas) using a thermal conductivity detector (TCD). For each evaluation of H_2 generation, 200 μL of the headspace was injected into the GC and was quantified by a calibration plot to the internal hydrogen standard. During the long-time stability measurements, the reaction system used N_2 to remove the produced hydrogen after every 4 h of irradiation, and the sacrificial agent remained unchanged.

The quantum efficiency (QE) of H_2 evolution was measured under conditions similar to the above photocatalytic reaction, except that the light source was equipped with a band-pass filter (420 nm). The photon flux of incident light was determined using a Ray virtual radiation actinometer (Apogee MQ-500, silicon ray detector, light spectrum, 389–692 nm; measurement range, 0–4000 $mol^{-1}\ m^{-2}\ s^{-1}$). The following equation (1) was used to calculate the quantum efficiency (QE).[40]

$$QE(\%) = \frac{n(H_2) \times 2}{n(\text{photons})} \times 100 \quad (1)$$

where $n(H_2)$ and n(photons) refer to the number of H_2 gas generated and the number of incident photons, respectively.

2.5 Photoelectrochemical measurements

The photoelectrochemical measurements were conducted on a CHI660E electrochemical workstation (Chenhua Instrument, Shanghai, China) in a conventional three-electrode system using the prepared FTO as the working electrode, Pt foil as the counter electrode, and Ag/AgCl (3 M KCl) as a reference electrode. A 0.1 M Na_2S/Na_2SO_3 aqueous solution was employed as the electrolytes, and a 300 W Xe lamp (Beijing China Education Au-light Co., Ltd) with a UV-cutoff filter (>380 nm) served as the solar simulator. Amperometric *I–t* curves were obtained by applying a bias potential of −0.2 V under chopped light irradiation with an ON/OFF interval of 25 s. Electrochemical impedance spectroscopy (EIS) measurements were conducted by applying a Zahner IM6 (Zahner Elektrik, Kronach, Germany) in the dark within a frequency range of 10^{-1}–10^4 Hz, and the amplitude sine wave potential was 10 mV in each case. Mott–Schottky plots were measured using the same three-electrode system in 0.2 M Na_2SO_4 aqueous solution. The above working electrode was prepared by mixing 5 mg photocatalyst with 5 μL Nafion and 0.4 mL ethanol to make slurry. Afterwards, the slurry (0.2 mL) was then coated onto the pretreated FTO glass (a 1.0 cm^2 active area). Finally, the resulting electrode was dried in air and heated in an oven at 60 °C for 1 h. To convert the obtained potential (*vs.* Ag/AgCl) to RHE (NHE at pH = 0), the following relationship was used:

$$E_{RHE} = E_{(Ag/AgCl)} + 0.059pH + E^0_{(Ag/AgCl)},$$

$$E^0_{(Ag/AgCl)} = 0.1967\ V.$$

3. Results and discussion

The controlled fabrication process of CdS@BDC NSs was schematically presented in Fig. 1a. First, uniform ultrathin Cd-MOF NSs were obtained by a solvothermal reaction of Cd^{2+} ions with 1,4-benzenedicarboxylic acid (H_2BDC), as shown in Fig. 1b. The corresponding AFM image and height profile intuitively exhibits their average thickness of *ca.* 1.46 nm (Fig. 1c). Then, the as-synthesized Cd-MOF NSs were transformed into CdS@BDC NSs *via* an *in situ* sulfidation method in Na_2S/Na_2SO_3 solution. Intriguingly, compared with their Cd-MOF precursors, the overall morphology of the nanosheet framework remains basically unchanged as shown in Fig. 1d. Furthermore, the nanosheet framework was uniformly embedded with *in situ* CdS nanoparticles, and the average size of the CdS nanoparticles is about 6 nm (Fig. 1e and f). The corresponding lattice spacing value (Fig. 1g) measured as 0.34 nm corresponded to the (111) facet of

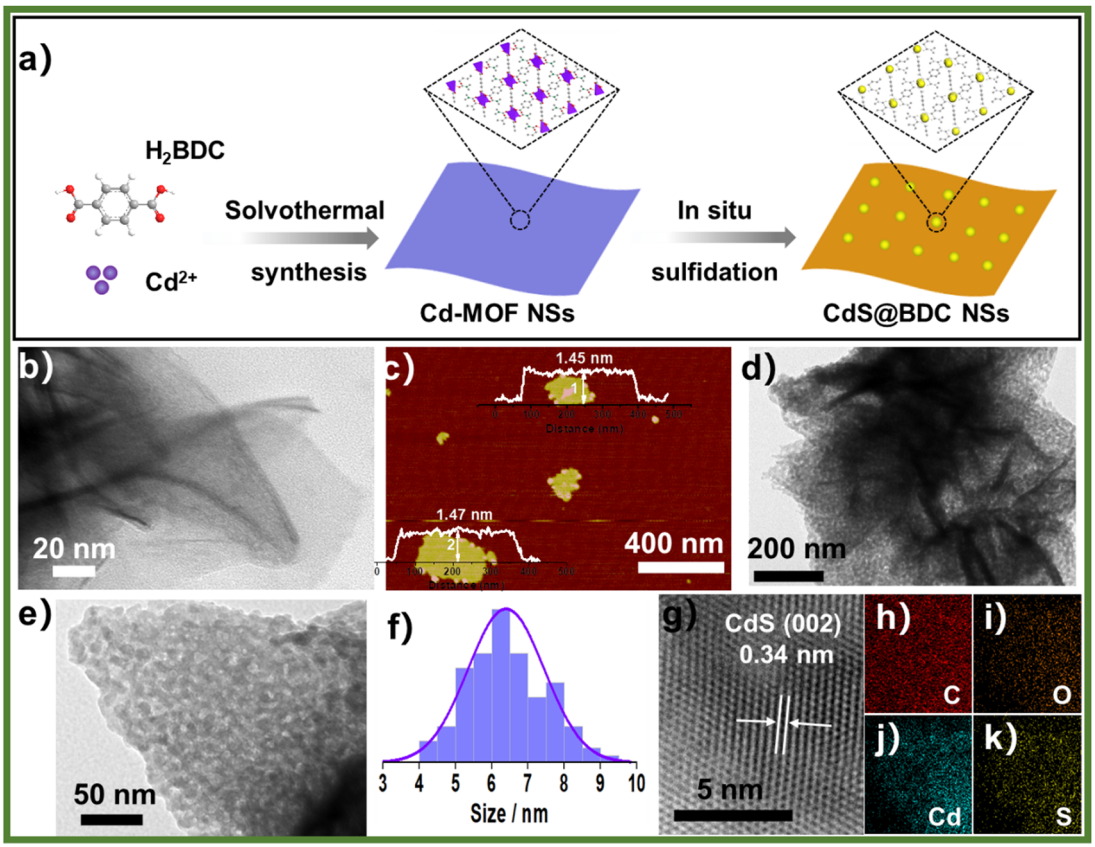

Fig. 1 (a) Schematic illustration of the synthesis process of CdS@BDC NSs. (b) TEM image of Cd-MOF NSs. (c) AFM image of Cd-MOF NSs and the corresponding height profiles (inset). (d and e) TEM images and particle size distribution (f) of CdS@BDC NSs. (g) HRTEM graph of CdS@BDC NSs. (h–k) Elemental mapping images of C, O, Cd and S recorded from the same region of the CdS@BDC NSs.

cubic-structured CdS.[41] The elemental mapping images (Fig. 1g–k) clearly depicted the uniform distribution of all elements (C, O, Cd, S) in their chemical composition, indicating that CdS@BDC NS is a homogeneous compound.

The structure and chemical state of the as-synthesized CdS@BDC NSs were further measured by PXRD and XPS. As shown in Fig. 2a, all of the diffraction peaks in the pattern of the Cd-MOF sample agreed well with the simulated XRD pattern of Cd-MOF ($[Cd(BDC)\text{-}(DMF)]^n$) with a space group $P1(-)(2)$ on the basis of the reported crystal structure data.[42] After *in situ* sulfidation treatment, the cubic-structured CdS phase was successfully obtained (JCPDS no. 10-0454).[43] Meanwhile, the corresponding EDX spectroscopy measurement revealed that the molar ratio of Cd/S is 1 : 1.07 in CdS@BDC NSs (Fig. S1, ESI†). As displayed in Fig. 2b, the XPS survey spectrum of the CdS@BDC NSs indicated the existence of Cd, S, as well as C and O from the nanosheet framework. From the high-resolution XPS spectrum of Cd 3d (Fig. 2b), the binding energies of Cd $3d_{5/2}$ (405.1 eV) and Cd $3d_{3/2}$ (411.9 eV) peaks, demonstrating the valences of Cd were +2 in CdS@BDC NSs, while the S 2P core level spectra (Fig. 2c) consisted of a doublet located at a binding energy of 161.3 eV and 162.5 eV, ascribing to the characteristic peaks of S $2p_{1/2}$ and S $2p_{3/2}$ spin–orbit components of S^{2-}, respectively.[44] All these indicated and

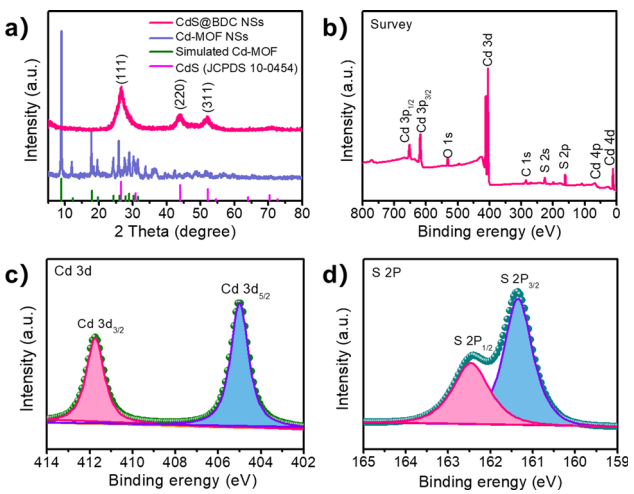

Fig. 2 (a) Powder XRD Profiles for Cd-MOF NSs and CdS@BDC NSs. (b) XPS survey spectra of the CdS@BDC NSs, the high-resolution XPS spectra of Cd 3d (c) and S 2p (d) XPS spectra of CdS@BDC NSs.

further confirmed the formation of a homogeneous CdS@BDC compound. According to the N_2 adsorption/desorption isotherms (Fig. 3a), it is clearly seen that a sharp increase at P/P^0 of 0.8–1.0, indicating typical type III isotherms,[45] and the SBET

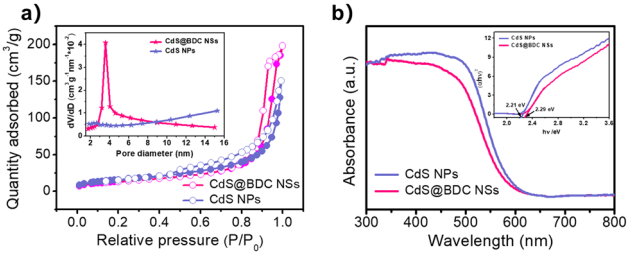

Fig. 3 (a) Nitrogen adsorption/desorption isotherms of the CdS@BDC NSs and CdS NPs (the inset exhibits corresponding pore size distribution curves). (b) UV-vis diffuse absorption spectra and their calculated band gap (inset) of the CdS@BDC NSs and CdS NPs.

of CdS@BDC NSs is 13.7 $m^2\ g^{-1}$. The UV-vis diffuse reflectance spectra (DRS UV-vis, Fig. 3b) of CdS@BDC NSs and CdS NPs (Fig. S2, ESI†) indicate that their comparable absorption edges are very close, ranging from 300 nm to 650 nm. The corresponding band gap values of CdS@BDC NSs and CdS NPs are also similar, corresponding to 2.29 eV and 2.21 eV estimated from the $(\alpha h\nu)^2$ *versus* photon energy ($h\nu$) plot (Fig. 3b, inset). The Mott–Schottky plots were also measured in 0.2 M Na_2SO_4 electrolyte with a pH value of 6.8. The positive slope of the C^{-2}–E plot (Fig. S3, ESI†) revealed the n-type semiconductor property of CdS@BDC NSs and CdS NPs.[46] The flat-band potential (V_{fb}) of CdS@BDC NSs and CdS NPs were −0.48 V and −0.41 V *vs.* Ag/AgCl (−0.21 V and −0.28 V *vs.* NHE) through extrapolating the intercept to the *X*-axis. For many n-type semiconductors, it is reported that the bottom of the conduction band (CB) potential is more negative by 0.1 V than the flat-band potential.[47] Thus, the CBs of the CdS@BDC NSs and CdS NPs were calculated to be −0.38 V and −0.31 V *vs.* NHE, respectively, exhibiting that the CB potential of the CdS@BDC NSs is more negative than that of CdS NPs, which is helpful for photocatalytic H_2 generation.

The photocatalytic hydrogen evolution was conducted under visible-light irradiation ($\lambda > 380$ nm) using S^{2-}/SO_3^{2-} as sacrificial reagents without the use of precious co-catalysts of Pt. CdS nanoparticles (NPs) (Fig. S2, ESI†) and CdS quantum dots (QDs) (Fig. S4, ESI†) were also evaluated as photocatalysts for reference. From Fig. 4a, it can be found that CdS NPs and CdS QDs have a H_2-evolution rate (HER) of 199 μmol $h^{-1}\ g^{-1}$ and 760 μmol $h^{-1}\ g^{-1}$, respectively. Prominently, the hydrogen production rate of CdS@BDC NSs is 13081 μmol $h^{-1}\ g^{-1}$, and is 65 times and 17 times that of CdS NPs and CdS QDs, respectively. The excellent hydrogen production performance shows that CdS@BDC NS is one of the most promising noble-metal-free CdS-based photocatalysts (Table S1, ESI†). Photocatalytic quantum efficiency QE of the CdS-based photocatalyst and previously reported CdS-based photocatalyst is listed in Table S2 (ESI†). Therefore, the QE of CdS@BDC NS (4.61%) is higher than that of CdS NP (0.63%) and CdS QD (1.37%), respectively. In addition, the photocatalytic quantum efficiency of CdS@BDC NS also seems to be higher than that of some precious metal-free photocatalysts based on CdS (*e.g.*, CdS/g C_3N_4, CdS/Cu_7S_4/g-$C_3N_4$and CdS/$NiSe_2$). The corresponding photostability of the CdS@BDC NSs was investigated *via* repeating the H_2-evolution experiments under the same experimental conditions, as illustrated in Fig. 4b. During four repeated photocatalytic experiments, no obvious reduction of hydrogen production was observed, implying its excellent photocatalytic stability. After four experimental cycles, the TEM image (Fig. S5a, ESI†) and PXRD patterns (Fig. S5b, ESI†) showed no significant changes in CdS@BDC NSs.

As we know, the efficiency of photogenerated carrier capture, separation and migration may play a crucial role in photocatalytic water splitting for H_2 evolution. It can be seen from Fig. 5a that the peak intensity of photoluminescence (PL) of CdS@BDC NSs is much weaker than that of CdS NPs, indicating that the recombination of photoinduced electron–hole (e–h) pairs in CdS@BDC NSs is more efficiently repressed.[48,49] Moreover, as displayed in the time-resolved PL spectra (Fig. 5b and Table S3, ESI†), the average photogenerated carrier lifetime of CdS@BDC NSs is 0.035 ns, which is longer than that of CdS NPs (0.021 ns), declaring that more photoelectrons can be used effectively for proton reduction.[50,51] The transient photocurrent–time curves (Fig. 5c) also reveal that the photocurrent density of CdS@BDC NSs has been substantially improved compared with CdS NPs, suggesting faster charge separation and higher efficiency of photogenerated electron–hole pairs.[36] In addition,

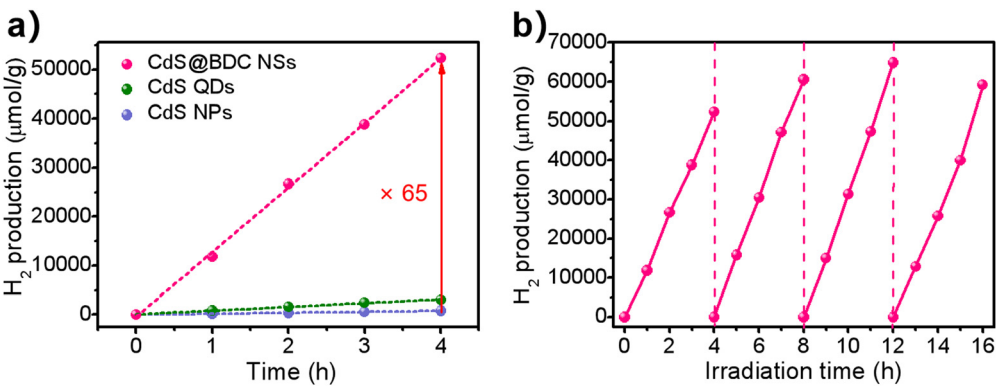

Fig. 4 (a) Comparison of the photocatalytic H_2-evolution activities of CdS@BDC NSs, CdS QDs and CdS NPs. (b) Cycling stability for the CdS@BDC NS photocatalysts.

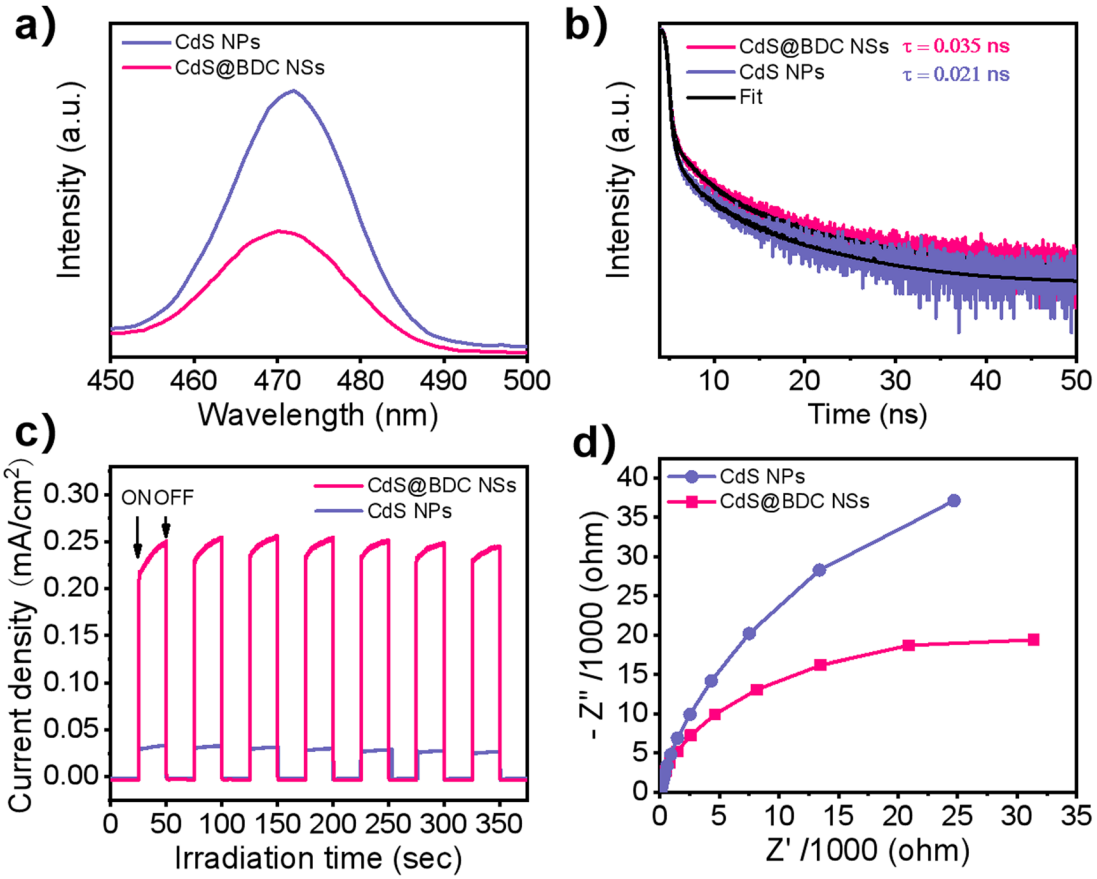

Fig. 5 (a) Photoluminescence spectra. (b) Time-resolved photoluminescence decay spectra. (c) Photocurrent response. (d) Electrochemical impedance spectra for the CdS@BDC NSs and CdS NPs.

as shown in Fig. 5d, the Nyquist plot of electrochemical impedance spectroscopy exhibits a smaller radius of CdS@BDC NSs than that of CdS NPs, corresponding to the lower charge-transport resistance.[24,52] Evidently, CdS@BDC NSs have the above-mentioned excellent photoelectrochemical properties due to their special 2-dimensional lamellar structure, thus obtaining a high photocatalytic hydrogen production rate. What's more, when another lactic acid solution replaced Na_2S/Na_2SO_3 solution as a hole sacrificing agent, the hydrogen production performance of CdS@BDC NSs was lower than that of conventionally synthesized CdS NPs (Fig. S6, ESI†). This strongly indicated that the presence of the Na_2S/Na_2SO_3 system also had a crucial impact on the hydrogen production performance. According to the FT-IR spectra of CdS@BDC NSs (Fig. S7, ESI†), there are the characteristic peaks of S^{2-} at 533 cm^{-1} and SO_3^{2-} at 1440 cm^{-1}. Meanwhile, the unwashed CdS NP sample was taken out of Na_2S/Na_2SO_3 solution, and the two absorption peaks were very weak. Obviously, after separation of the suspensible CdS@BDC NS from sulfur-rich S^{2-}/SO_3^{2-} solution, the resultant sample shows the highest various absorption peaks including the adsorbed S^{2-} and SO_3^{2-}, and the selective adsorption of massive S^{2-} ions on the CdS@BDC NSs surface.

On the basis of the above results, a tentative photocatalytic mechanism for the enhanced hydrogen production performance over CdS@BDC NSs was proposed in Fig. 6. In this work, a very important feature is that MOF-derived CdS@BDC NSs can efficiently adsorb a larger amount of S^{2-}/SO_3^{2-} compared with the traditional CdS NPs (Fig. S7, ESI† and Fig. 6A). Then, due to the two-dimensional skeleton structure on the surface of CdS@BDC NSs and a large number of exposed S^{2-} ions, this supported the photo-excited electrons and holes to migrate to the spatially separated reduction center (at the small edge) and oxidation center (at the large base surface).53 On one hand, it is well known that S^{2-}/SO_3^{2-} has been widely used as an excellent sacrificial reagent for effectively consuming photogenerated holes in the photocatalytic H_2 evolution of CdS photocatalysts, in which S^{2-} ions can be oxidized into solid S^0 by photogenerated holes at first, and then converted into $S_2O_3^{2-}$ ions together with SO_3^{2-} (Fig. 6B). The depletion of holes will inhibit the recombination of photogenerated electrons and holes, and as a result, more photoelectrons can be effectively used for proton reduction. This is also confirmed by the above photoluminescence spectrum and time-resolved luminescence decay spectrum analysis results shown in Fig. 5a and b. On the other hand, massive S^{2-} adsorbed on the surface of ultrathin CdS@BDC NSs can also be exposed as interfacial hydrogen evolution active sites (also known as electronic co-catalysts), which can enrich H^+ ions from sacrificial agent solution and subsequently reduce H^+ to H_2 through

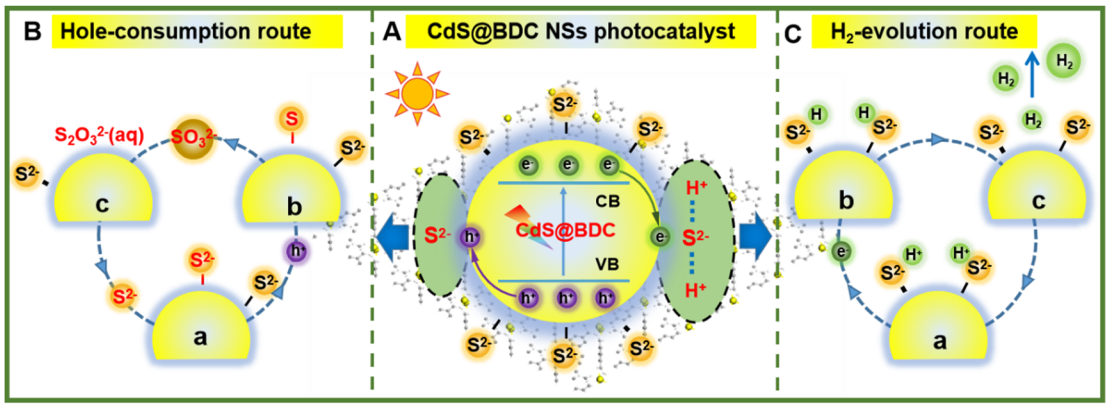

Fig. 6 Schematic illustration of the S^{2-}-mediated mechanism in CdS@BDC NSs: (A) S^{2-}-mediated interfacial charge transfer and separation in the CdS@BDC NSs, (B) hole-consumption route by S^{2-}/SO_3^{2-} ions, and (C) H_2-evolution reaction route on the adsorbed S^{2-} ions as the catalytic active sites.

photoelectrons for promoting the hydrogen production reaction (Fig. 6C).[54,55] Therefore, numerous S^{2-}/SO_3^{2-} ions adsorbed on the surface of CdS@BDC NSs can not only act as a hole-scavenger to promote the rapid capture and consumption of photogenerated holes, but also serve as an active site for catalytic reaction, and synergistically enhance the photocatalysis hydrogen production performance. That is to say, CdS in CdS@BDC NSs is the catalytic center, while BDC mainly plays an auxiliary role in the framework. Moreover, BDC with a porous structure assisted CdS to form an ultra-thin structure similar to complex, which made a large amount of S^{2-}/SO_3^{2-} adsorbed on the surface, thus removing a large amount of photo-generated holes and inhibiting the photo-corrosion of CdS. When another lactic acid solution replaces Na_2S/Na_2SO_3 solution as the hole sacrificial agent, the hydrogen production performance of CdS@BDC NSs is lower than that of the conventionally synthesized CdS NPs (Fig. S6, ESI†). Because lactic acid molecules can't be enriched on the surface of CdS in CdS@BDC NSs due to the steric hindrance and the adsorption effect, which leads to a sharp decrease in performance, it helps to verify the structural function of CdS@BDC NSs.

In view of the above research on the synthesis method and hydrogen production performance of CdS@BDC NSs, it is speculated that this synthesis strategy and the corresponding photocatalytic enhancement mechanism are also universal in other 2D MOF-based nanomaterials. Therefore, we further synthesized Zn-MOF NSs and the corresponding ZnS@BDC NSs (Fig. S8a–d, ESI†). As a comparison, traditional ZnS NPs were also synthesized. As shown in Fig. S9 (ESI†), compared with traditional ZnS NPs (101 μmol h^{-1} g^{-1}), ZnS@BDC NSs exhibit a substantial increase in photocatalytic hydrogen production activity of 2801 μmol h^{-1} g^{-1}. Hence, our proposed synthesis method and the corresponding enhancement mechanism of photocatalytic hydrogen evolution can be used as an effective method to develop new efficient hydrogen production photocatalysts.

4. Conclusions

In summary, we have successfully prepared ultrathin CdS@BDC nanosheet photocatalysts *via in situ* sulfidation treatment from a precursor of 2D Cd-MOF nanosheets. In this case, due to the porous structure and larger surface area of the synthesized CdS@BDC NSs derived from the 2D Cd-MOF, a large number of S^{2-} ions can be rapidly enriched to its surface, preventing light corrosion and acting as an active site of the surface catalytic reaction. It was proposed that the resultant CdS@BDC NS photocatalysts exhibited a perfect hydrogen generation activity of 13 081 μmol h^{-1} g^{-1}, which was about 65 times higher than that of CdS NPs. In addition, a tentative photocatalytic mechanism for the enhanced hydrogen production performance over CdS@BDC NSs was also proposed. Our work not only provides a facile and effective method for the synthesis of highly efficient photocatalysts, but also opens up new insight for the application of 2D MOF-based nanomaterials in photocatalysis.

Author contributions

Jian Li: conceptualization, investigation, formal analysis, data curation, validation, and writing – review and editing. Huaqiang Wang: conceptualization, investigation, formal analysis, data curation, methodology, and writing – original draft. Yihong Gao: theoretical calculation. Hao Fang: methodology and investigation. Peiyu Chen: formal analysis and performed the theoretical calculations. Fangzhi Huang: conceptualization, data curation, formal analysis, funding acquisition, resources, and supervision.

Conflicts of interest

There are no conflicts to declare.

Acknowledgements

This work was supported by the National Natural Science Foundation of China (no. 21771001, 51872002, and 21371002), the key research and development projects in Anhui Province (202004a07020026), and the Key Lab of Photovoltaic and Energy Conservation Materials, Chinese Academy of Sciences, which is gratefully acknowledged by the authors.

References

1 S. B. Wang, B. Y. Guan and X. W. D. Lou, *J. Am. Chem. Soc.*, 2018, **140**, 5037–5040.
2 J. R. Ran, W. W. Guo, H. L. Wang, B. C. Zhu, J. G. Yu and S. Z. Qiao, *Adv. Mater.*, 2018, **30**, 1800128.
3 J. R. Ran, B. C. Zhu and S.-Z. Qiao, *Angew. Chem., Int. Ed.*, 2017, **56**, 10373–10377.
4 K. Yang, X. X. Li, C. L. Yu, D. B. Zeng, F. Y. Chen, K. L. Zhang, W. Y. Huang and H. B. Ji, *Chin. J. Catal.*, 2019, **40**, 796–818.
5 Z. X. Qin, Z. X. Huang, M. L. Wang, D. Y. Liu, Y. B. Chen and L. J. Guo, *Appl. Catal., B*, 2020, **261**, 118211.
6 J. Cao, H. Wang, Y. Zhao, Y. Liu, Q. Wu, H. Huang, M. Shao, Y. Liu and Z. Kang, *J. Mater. Chem. A*, 2020, **8**, 3701–3707.
7 A. Fujishima and K. Honda, *Nature*, 1972, **238**, 37–38.
8 N. Tian, Y. H. Zhang, X. W. Li, K. Xiao, X. Du, F. Dong, G. I. N. Waterhouse, T. R. Zhang and H. W. Huang, *Nano Energy*, 2017, **38**, 72–81.
9 W. Wang, G. Li, T. An, D. K. L. Chan, J. C. Yu and P. K. Wong, *Appl. Catal., B*, 2018, **238**, 126–135.
10 C. Lai, M. M. Zhang, B. S. Li, D. L. Huang, G. M. Zeng, L. Qin, X. G. Liu, H. Yi, M. Cheng, L. Li, Z. Chen and L. Chen, *Chem. Eng. J.*, 2019, **358**, 891–902.
11 K. K. Dey, S. Gahlawat and P. P. Ingole, *J. Mater. Chem. A*, 2019, **7**, 21207–21221.
12 T.-D. Pham, B.-K. Lee, V. N. Nguyen and V.-D. Dao, *J. Catal.*, 2017, **352**, 13–21.
13 M. Xiao, B. Luo, M. Lyu, S. Wang and L. Wang, *Adv. Energy Mater.*, 2018, **8**, 1701605.
14 J. Wu, W. Xia, M. H. Lan, X. J. Xing, J. C. Hu, L. Huang, J. Liu, Y. Y. Ren, H. F. Liu and F. Wang, *J. Mater. Chem. A*, 2020, **8**, 21690.
15 X. M. Ning, Y. L. Wu, X. F. Ma, Z. Zhang, R. Q. Gao, J. Chen, D. L. Shan and X. Q. Lu, *Adv. Funct. Mater.*, 2019, **29**, 1902992.
16 C. Zhu, C. Liu, Y. J. Zhou, Y. J. Fu, S. J. Guo, H. Li, S. Q. Zhao, H. Huang, Y. Liu and Z. H. Kang, *Appl. Catal., B*, 2017, **216**, 114–121.
17 G. T. Sun, S. M. Mao, D. D. Ma, Y. J. Zou, Y. X. Lv, Z. H. Li, C. He, Y. H. Cheng and J.-W. Shi, *J. Mater. Chem. A*, 2019, **7**, 15278–15287.
18 J. C. Hu, S. S. Sun, M. D. Li, W. Xia, J. Wu, H. F. Liu and F. Wang, *Chem. Commun.*, 2019, **55**, 14490.
19 T. Xiong, H. Wang, Y. Zhou, Y. J. Sun, W. L. Cen, H. W. Huang, Y. X. Zhang and F. Dong, *Nanoscale*, 2018, **10**, 8066–8074.
20 P. Wang, Y. Sheng, F. Z. Wang and H. G. Yu, *Appl. Catal., B*, 2018, **220**, 561–569.
21 D. P. Kumar, S. Hong, D. A. Reddy and T. K. Kim, *Appl. Catal., B*, 2017, **212**, 7–14.
22 Y. J. Hao, S.-Z. Kang, X. Liu, X. Q. Li, L. X. Qin, J. Mu and A. C. S. Sustainable, *Chem. Eng.*, 2016, **5**, 1165–1172.
23 A. Kudo and Y. Miseki, *Chem. Soc. Rev.*, 2009, **38**, 253–278.
24 J.-D. Xiao and H.-L. Jiang, *Small*, 2017, **13**, 1700632.
25 J.-X. Lv, Z.-M. Zhang, J. Wang, X.-L. Lu, W. Zhang and T.-B. Lu, *ACS Appl. Mater. Interfaces*, 2018, **11**, 2655–2661.
26 D. D. Ma, J.-W. Shi, Y. J. Zou, Z. Y. Fan, X. Ji and C. M. Niu, *ACS Appl. Mater. Interfaces*, 2017, **9**, 25377–25386.
27 H. X. Deng, S. Grunder, K. E. Cordova, C. Valente, H. Furukawa, M. Hmadeh, F. Gándara, A. C. Whalley, Z. Liu, S. Asahina, H. Kazumori, M. O'Keeffe, O. Terasaki, J. F. Stoddart and O. M. Yaghi, *Science*, 2012, **336**, 1018–1023.
28 M. Eddaoudi, J. Kim, N. Rosi, D. Vodak, J. Wachter, M. O'Keeffe and O. M. Yaghi, *Science*, 2002, **295**, 469–474.
29 B. L. Zhu, B. Z. Lin, Y. Zhou, P. Sun, Q. R. Yao, Y. L. Chen and B. F. Gao, *J. Mater. Chem. A*, 2014, **2**, 3819–3827.
30 C. L. Tan and H. Zhang, *Chem. Soc. Rev.*, 2015, **44**, 2713–2731.
31 Q. Wang and D. O'Hare, *Chem. Rev.*, 2012, **112**, 4124–4155.
32 S. K. Muduli, E. Varrla, Y. Xu, S. A. Kulkarni, A. Katre, S. Chakraborty, S. Chen, T. C. Sum, R. Xu and N. Mathews, *J. Mater. Chem. A*, 2017, **5**, 24874–24879.
33 D. D. Zhu, J. L. Liu, Y. Q. Zhao, Y. Zheng and S. Z. Qiao, *Small*, 2019, **15**, 1805511.
34 B. Han, X. W. Ou, Z. Q. Deng, Y. Song, C. Tian, H. Deng, Y.-J. Xu and Z. Lin, *Angew. Chem., Int. Ed.*, 2018, **57**, 16811–16815.
35 Y. Huang, M. T. Zhao, S. K. Han, Z. C. Lai, J. Yang, C. L. Tan, Q. L. Ma, Q. Q. Lu, J. Z. Chen, X. Zhang, Z. C. Zhang, B. Li, B. Chen, Y. Zong and H. Zhang, *Adv. Mater.*, 2017, **29**, 1700102.
36 J. R. Ran, J. T. Qu, H. P. Zhang, T. Wen, H. L. Wang, S. M. Chen, L. Song, X. L. Zhang, L. Q. Jing, R. K. Zheng and S. Z. Qiao, *Adv. Energy Mater.*, 2019, **9**, 1803402.
37 Q. P. Lu, M. T. Zhao, J. Z. Chen, B. Chen, C. L. Tan, X. Zhang, Y. Huang, J. Yang, F. F. Cao, Y. F. Yu, J. F. Ping, Z. C. Zhang, X. J. Wu and H. Zhang, *Small*, 2016, **12**, 4669–4674.
38 Y. F. Lin, G. Chen, H. Wan, F. S. Chen, X. H. Liu and R. Z. Ma, *Small*, 2019, **15**, 1900348.
39 R.-B. Wei, Z.-L. Huang, G.-H. Gu, Z. Wang, L. X. Zeng, Y. B. Chen and Z.-Q. Liu, *Appl. Catal., B*, 2018, **231**, 101–107.
40 W. C. Wang, Y. Tao, J. C. Fan, Z. P. Yan, H. Shang, D. L. Phillips, M. Chen and G. S. Li, *Adv. Funct. Mater.*, 2022, **32**, 2201357.
41 W. L. Zhen, X. F. Ning, B. J. Yang, Y. Q. Wu, Z. Li and G. X. Lu, *Appl. Catal., B*, 2018, **221**, 243–257.
42 A. D. Burrows, K. Cassar, T. Düren, R. M. W. Friend, M. F. Mahon, S. P. Rigby and T. L. Savarese, *Dalton Trans.*, 2008, 2465–2474.
43 X. F. Ning, S. G. Meng, X. L. Fu, X. G. Ye and S. F. Chen, *Green Chem.*, 2016, **18**, 3628–3639.
44 G. D. Yang, B. L. Yang, T. C. Xiao and Z. F. Yan, *Appl. Surf. Sci.*, 2013, **283**, 402–410.
45 X. X. Zhao, J. R. Feng, J. Liu, W. Shi, G. M. Yang, G. C. Wang and P. Cheng, *Angew. Chem., Int. Ed.*, 2018, **57**, 9790–9794.

46 Y. J. Xiao, Y. Qi, X. L. Wang, X. Y. Wang, F. X. Zhang and C. Li, *Adv. Mater.*, 2018, **30**, 1803401.
47 Y. Matsumoto, *J. Solid State chem.*, 1996, **126**, 227–234.
48 S. Thaweesak, M. Q. Lyu, P. Peerakiatkhajohn, T. Butburee, B. Luo, H. J. Chen and L. Wang, *Appl. Catal., B*, 2017, **202**, 184–190.
49 M. Ou, W. G. Tu, S. M. Yin, W. N. Xing, S. Y. Wu, H. J. Wang, S. P. Wan, Q. Zhong and R. Xu, *Angew. Chem., Int. Ed.*, 2018, **130**, 13758–13762.
50 F. Raziq, L. Q. Sun, Y. Y. Wang, X. L. Zhang, M. Humayun, S. Ali, L. L. Bai, Y. Qu, H. T. Yu and L. Q. Jing, *Adv. Energy Mater.*, 2018, **8**, 1701580.
51 J. Bian, Y. Qu, X. L. Zhang, N. Sun, D. Y. Tang and L. Q. Jing, *J. Mater. Chem. A*, 2018, **6**, 11838–11845.
52 M. Zhou, S. B. Wang, P. J. Yang, C. J. Huang and X. C. Wang, *ACS Catal.*, 2018, **8**, 4928–4936.
53 N. F. Wang, S. Cheong, D. E. Yoon, P. Lu, H. J. Lee, Y. K. Lee, Y. S. Park and D. C. Lee, *J. Am. Chem. Soc.*, 2022, **144**(37), 16974–16983.
54 H. G. Yu, W. Zhong, X. Huang, P. Wang and J. G. Yu, *ACS Sustain. Chem. Eng.*, 2018, **6**, 5513–5523.
55 W. Zhong, X. Huang, Y. Xu and H. G. Yu, *Nanoscale*, 2018, **10**, 19418–19426.